

Observation of a phononic quadrupole topological insulator

Marc Serra-Garcia,^{1,*} Valerio Peri,^{1,*} Roman Süsstrunk,¹ Osama R. Bilal,^{1,2} Tom Larsen,³ Luis Guillermo Villanueva,³ and Sebastian D. Huber¹

¹*Institute for Theoretical Physics, ETH Zurich, 8093 Zürich, Switzerland*

²*Division of Engineering and Applied Science, California Institute of Technology, Pasadena, CA 91125, USA*

³*Advanced NEMS Group, École Polytechnique Fédérale de Lausanne (EPFL), 1015 Lausanne, Switzerland*

(Dated: August 28, 2020)

The modern theory of charge polarization in solids^{1,2} is based on a generalization of Berry's phase.³ Its possible quantization^{4,5} lies at the heart of our understanding of all systems with topological band structures that were discovered over the last decades.^{6–10} While based on the concept of the “charge” polarization, the same theory can be used as an elegant tool to characterize the Bloch bands of neutral bosonic systems such as photonic¹¹ or phononic crystals.^{12,13} Recently, the theory of this quantized polarization was extended from the dipole- to higher multipole-moments.¹⁴ In particular, a two-dimensional quantized quadrupole insulator is predicted to have gapped yet topological one-dimensional edge-modes, which in turn stabilize zero-dimensional in-gap corner states.¹⁴ However, such a state of matter has not been observed experimentally. Here, we provide the first measurements of a phononic quadrupole insulator. We experimentally characterize the bulk, edge, and corner physics of a mechanical metamaterial and find the predicted gapped edge and in-gap corner states. We further corroborate our findings by comparing the mechanical properties of a topologically non-trivial system to samples in other phases predicted by the quadrupole theory. From an application point of view, these topological corner states are an important stepping stone on the way to topologically protected wave-guides^{12,15} in higher dimensions and thereby open a new design path for metamaterials.^{16,17}

A non-vanishing dipole moment $\mathbf{p} = \langle \Psi | \mathbf{r} | \Psi \rangle$ in an insulator does not lead to any charge accumulation in the bulk. However, it manifests itself through uncompensated surface charges and hence induces potentially interesting surface physics, see Fig. 1a. The dipole moment \mathbf{p} is expressible through Berry's phase,^{1,3} which in turn can lead to its quantization.^{4,5,18–21} All observed topological insulators fit into this framework of quantized dipole moments,⁴ or mathematical generalizations thereof.²¹ Moreover, for neutral systems, the abstract quantity \mathbf{p} loses its electromagnetic content. However, it can equally well be used to predict band-structure effects such as stable surface modes. Whether higher order moments, such as the quadrupole, can lead to distinctly new topological phases of matter remained unclear.

Recently, a theory for a quantized quadrupole insulator was put forward¹⁴ based on its phenomenology: A bulk

quadrupole moment in a finite two-dimensional sample gives rise to surface dipole moments on its one-dimensional edges as well as to uncompensated charges on the zero-dimensional corners, see Fig. 1b. The former is indicating *gapped edge modes* while the latter motivates the presence of *in-gap corner excitations*. This also defines the key technological use of such a quadrupole insulator in mechanical or optical metamaterials: The localized corner modes can be used for acoustic field enhancement in two dimensions.²² Moreover, these states serve

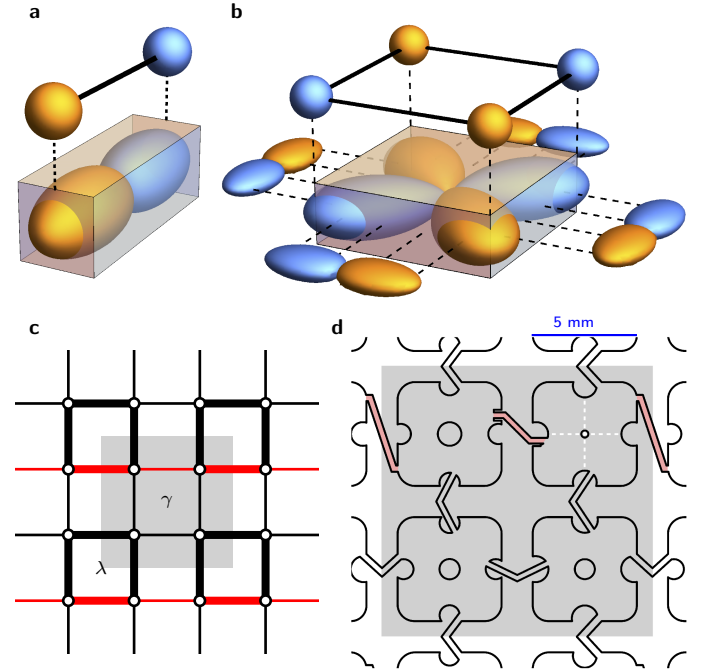


FIG. 1: **Quadrupole topological insulator** **a**, in a finite size system, a bulk dipole moment induces surface charges as illustrated by the spheres. **b**, A bulk quadrupole moment with its accompanying edge dipoles and corner charges. **c**, a concrete model for a system with a non-vanishing quadrupole moment. Thin (thick) lines denote weak (strong) hoppings with strength γ and λ respectively. The red (black) lines indicate a negative (positive) hopping amplitude resulting in a π -flux per plaquette. **d**, metamaterial design implementing the model in **c**. The out-of-plane plate-modes with two nodal lines (dashed white lines) are coupled via the bent beams. Beams connecting different sides of a nodal line (shaded red) mediate negative coupling matrix elements. The gray areas in **c** & **d** mark the unit cell of the tight-binding model.

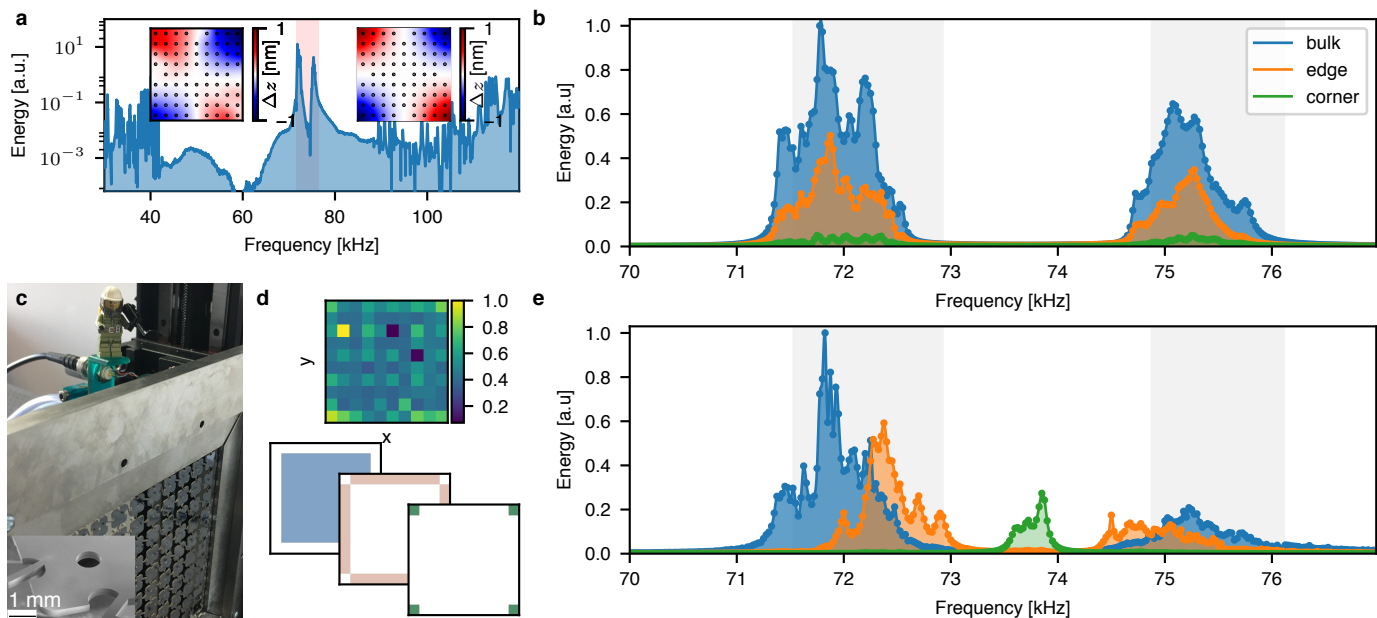


FIG. 2: **Quadrupole in-gap states** **a**, Spectrum on a single plate indicating the large separation between the targeted mode around 73.5 kHz (shaded red) and the bands above and below. The left inset shows the mode profile measured on a single plate (the black dots mark the measurement points used for the interpolation), whereas the right inset shows the numerically calculated mode profile. In **d**, the response of all plates at an arbitrary frequency (72.0 kHz) is shown. These images are then multiplied by the displayed filters to determine bulk, edge, and corner response. **b** and **e** show the resulting spectra for the trivial and non-trivial sample, respectively. For the trivial case, one can see two bands (the gray area indicates the theoretically predicted location of the two bands) and a central gap with no resonances. For all frequencies, the weights of the bulk (blue), edge (orange), and corner (green) responses follow their fraction of the total 10x10 system. The non-trivial case (**e**) shows bulk- and edge-dominated frequency-regions and strong corner peaks in the middle of the gap. **c**, Photo of the setup (inset: close-up of a single plate).

as a stepping stone towards topologically protected, one-dimensional channels in three dimensions: When appropriately stacked into three dimensions, the corner modes give rise to chiral one dimensional modes along edges of the three dimensional sample.^{17,23–26}

The phenomenology of gapped edges and gapless corners can be formalized mathematically. Benalcazar et al.¹⁴ proposed to use nested Wilson loops as a way to obtain a quantized quadrupole moment (see Methods for details): Wilson loop operators depend only on the bulk properties and encode the edge physics via their eigenvalues $\nu^\pm(k_\alpha)$, $\alpha = x, y$, known as Wannier bands.²⁷ If these Wannier bands $\nu^\pm(k_\alpha)$ are gapped, the eigenvectors of the Wilson loops can be used to define the bulk-induced edge polarization of the bands below the gap $p_\alpha^{\nu-}$, where α denotes the direction of the polarization. In the same way as for the conventional topological insulators,⁵ symmetries are required for the quantization of $p_\alpha^{\nu-}$. Particularly, the presence of inversion symmetry I and non-commuting mirror symmetries M_x and M_y lead to a well defined and quantized $p_\alpha^{\nu-} \in \{0, 1/2\}$. In particular, the sought after quantized quadrupole phase is described by¹⁴

$$(p_x^{\nu-}, p_y^{\nu-}) = (1/2, 1/2). \quad (1)$$

As a corner terminates two edges, $(p_x^{\nu-}, p_y^{\nu-}) = (1/2, 1/2)$ could suggest that each of them supports two in-gap states. However, it is an important hall-mark of the bulk nature

of the quadrupole insulator that each corner hosts only one mode, cf. Fig. 1b.¹⁴

A concrete tight-binding model for a two-dimensional quantized quadrupole insulator is shown in Fig. 1c.¹⁴ The dimerized hopping with amplitude λ and γ leads to a band-gap between two pairs of degenerate bands for $\lambda \neq \gamma$ (see Methods). The black (red) lines in Fig. 1c indicate positive (negative) hoppings, effectively emulating a magnetic π -flux per plaquette. This π -flux requires the mirror-symmetry around the horizontal axis (M_y) to be accompanied by a gauge-transformation, leading to the non-commutation of M_x and M_y . The present model also has inversion I and C_4 rotational symmetry (again up to a gauge-transformation) forcing $p_x^{\nu-} = p_y^{\nu-}$ as well as particle-hole symmetry fixing the corner modes to the middle of the gap. For $\gamma < \lambda$ the topological phase $(p_x^{\nu-}, p_y^{\nu-}) = (1/2, 1/2)$, whereas for $\gamma > \lambda$, the trivial phase $(0, 0)$ is realized.¹⁴ Here, we seek a mechanical implementation of a quadrupole insulator with $\ddot{x}_i = -\mathcal{D}_{ij}x_j$, where the dynamical matrix \mathcal{D}_{ij} couples local degrees of freedom x_i according to the model in Fig. 1c.

We implement the quadrupole insulator using the concept of perturbative mechanical metamaterials.²⁸ The starting point is a single-crystal silicon plate with dimensions $5 \times 5 \times 0.364$ mm, whose mechanical eigenmodes are described by the displacement field $\mathbf{u}(\mathbf{r})$. We work with the first non-rigid-body mode which is characterized by

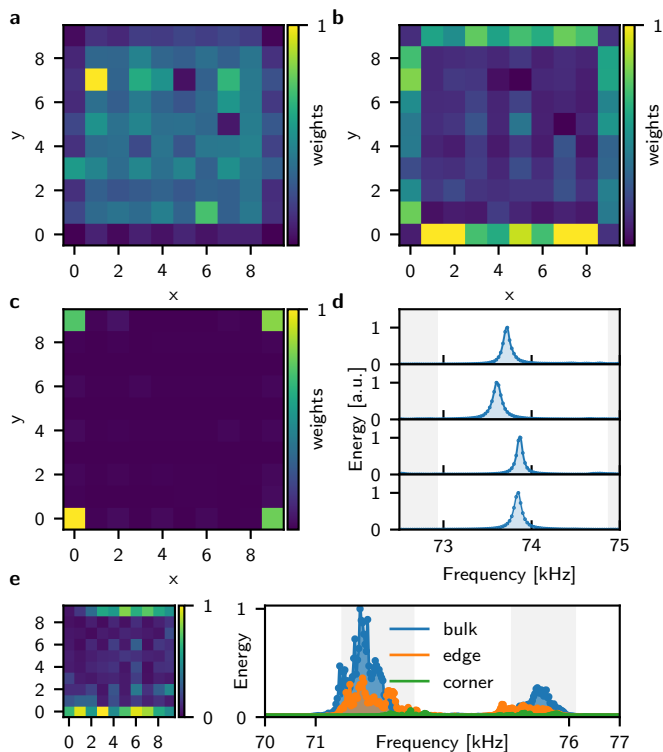


FIG. 3: **Edge and corner modes** **a – c**, Normalized integrated weights of the response of frequency regions in Fig. 1e where bulk (**a**), edge (**b**), and corner modes (**c**) dominate. **d**, Spectral response of the four corner sites in clock-wise arrangement starting from the top left corner. The combination of gapped edge modes on all four edges, see **b**, together with the single mode per corner evidences the quadrupole nature of our metamaterial. **e**, Spectrum and edge dominated modes of a system in the non-quadrupole phase $(p_x, p_y) = (1/2, 0)$ showing no corner states but surface modes on two of the four edges.

two perpendicular nodal lines in the out-of-plane component of $\mathbf{u}(\mathbf{r})$, see Fig. 1d and Fig. 2a. By spectrally separating this mode from the modes below and above it, one can describe the dynamics in some frequency range by specifying only the amplitude x_i of the mode of interest of a given plate i . The hopping elements in \mathcal{D}_{ij} are then implemented by thin beams between neighboring plates. The nodal structure of the mode allows to mediate couplings of either positive or negative sign, depending on which sides of the nodal lines are connected by the beams. Moreover, the distance to the nodal line controls the coupling strength mediated by a given beam. Combinatorial search²⁹ followed by a gradient optimization²⁸ leads to the design in Fig. 1d which is characterized by a ratio $|\gamma/\lambda| = 0.28$, or $|\lambda/\gamma| = 0.28$, see Methods.

All measurements shown are performed using the same scheme: The plates are excited with an ultrasound air-transducer. The transducer has a diameter of 5 mm and is in close proximity to the sample, such that only a single plate is excited. We measure the response of the excited plate with a laser-interferometer. In this way, we measure

the out-of-plane vibration amplitude $\Delta z_i \propto \psi_i^2$, where ψ_i is the eigenmode at the measured frequency (both the excitation strength and the measurement scale with ψ_i). The inset of Fig. 2a shows the local mode of a single plate measured in this way. In all other figures we display the mechanical energy $\varepsilon_i \propto \Delta z_i^2$.

To identify the in-gap states we take a measurement of $\varepsilon_i(\nu)$ as a function of frequency ν on all plates i . We then apply the filters $\varepsilon_\alpha(\nu) = \sum_i \varepsilon_i(\nu) F_{i,\alpha}$ shown in Fig. 2d to separate the response of the bulk, edges, and corners. Figs. 2b & e show the resulting spectra for two different samples (see Methods). In the topologically trivial case with $\gamma > \lambda$, one can observe two frequency bands where the system absorbs energy (the theoretically predicted location of the bands is indicated in gray). Two features characterize this trivial phase: (i) No frequency range is dominated by the edge or corner response. Moreover, the relative weight of the three curves is in good accordance with the respective number of sites in the bulk, edges, and corners, respectively. (ii) No resonances appear in the gap between 72.92 kHz and 74.89 kHz. For the sample with $\gamma < \lambda$ in Fig. 2e, two key-features of the quantized quadrupole phase appear: (i) close to 72.92 kHz and 74.89 kHz, the response is dominated by the edges, indicative of the bulk-induced gapped edge modes. (ii) Sharp resonances at the corners appear in the gap region. A small mirror symmetry breaking leads to the non-degeneracy of the in-gap states which we discuss below.

The spectra in Fig. 2b & e allow to identify three frequency regions \mathcal{B} , \mathcal{E} , and \mathcal{C} , where the bulk (blue), edge (orange), or corner (green) response dominates. To establish the quadrupole nature of the metamaterial, we analyze the site-dependent, frequency integrated response $\varepsilon_i^\alpha = \sum_{\nu \in \alpha} \varepsilon_i(\nu)$ with $\alpha = \mathcal{B}, \mathcal{E}, \mathcal{C}$. In Fig. 3a–c we show the resulting spatial profiles. Note that the bulk induces gapped edge-modes on all four sides of the sample.

The hallmark of the quadrupole phase lies in the counting of corner modes: Each corner terminates two-gapped edges, nevertheless, they all host only one in-gap mode.¹⁴ In Fig. 3d, we show the response $\varepsilon(\nu)$ for the four corner plates. The resonances in the four corners are split by the presence of next-to-nearest neighbor couplings that break the particle-hole symmetry. However, each corner hosts only one resonance peak. Moreover, measurements of the edge-Greens function further support this claim, see Methods.

To corroborate our claim of observing a quadrupole insulator, we further explore the phase diagram of Ref. 14. When the C_4 -symmetry is broken by allowing for different hoppings in x - and y -direction (see Methods), the phase $(p'_x, p'_y) = (1/2, 0)$ can be reached via a gap-closing of the surface modes. The $(1/2, 0)$ -phase is characterized by gapped edge spectra on two parallel edges and no emergent edge physics on the perpendicular surfaces.¹⁴ Moreover, the induced edge modes are in a trivial state and no corner charges are induced. In Fig. 3e, we show measurements on a sample in the $(1/2, 0)$ -phase, where no in-gap states appear and the frequency region dominated by the

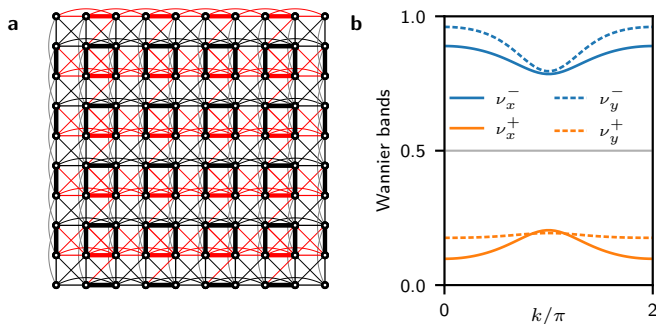


FIG. 4: **Reduced model and Wannier bands** **a**, Extracted reduced model for our design. Black (red) lines indicate positive (negative) couplings between the plate modes, whereas the thickness of the lines encodes the hopping amplitude. The unwanted next-to-nearest neighbor couplings arise from second-order effects involving other plate modes and break the M_x and M_y symmetries. **b**, Calculated Wannier bands from the model on the left.

edges draws its weight from only two surfaces.

In addition to the experimental data presented above, we also validate our system through extensive numerical calculations. The design process for the sample shown in Fig. 1d requires a finite-element simulation of the displacement fields $\mathbf{u}_i(\mathbf{r})$ on four unit cells containing a total of 16 sites i . The modes obtained in this way can then be projected onto the basis of uncoupled plate-modes $\mathbf{u}_i^0(\mathbf{r})$. In this way a reduced order model $\tilde{\mathcal{D}}_{ij}$ in the frequency range of the modes $\mathbf{u}_i^0(\mathbf{r})$ is obtained.²⁸ In Fig. 4a, we show the resulting model extended to a 10×10 system. The nearest neighbor couplings indeed follow the blueprint of the target model shown in Fig. 1c. However, spurious long-range couplings mediated by off-resonant admixing of other single-plate modes induce a certain amount of mirror-symmetry breaking. This is most notable in the

y -direction, where negative next-to-nearest neighbor couplings are mapped to positive ones, which is not corrected for in the gauge-transformation in M_y .

The reduced order model $\tilde{\mathcal{D}}_{ij}$ can also be used to calculate the topological indices (p'_x, p'_y) . The gapped Wannier bands $\nu_x^\pm(k_y)$ and $\nu_y^\pm(k_x)$ are shown in Fig. 4b. Note that the M_x symmetry implies $\nu_x^+(k_y) + \nu_x^-(k_y) = 1/2$ and the same for $x \leftrightarrow y$.¹⁴ The absence of an exact M_y symmetry indeed leads to a breaking of this rule. This is also reflected in the value of the polarizations

$$(p'_x, p'_y) = (0.50, 0.56). \quad (2)$$

As expected from the structure of $\tilde{\mathcal{D}}_{ij}$ shown in Fig. 4a, the polarizations are not precisely quantized. However, the phenomenology of in-gap corner modes is still observed as the symmetry breaking terms do not lead to any gap-closing, neither on the edge nor in the bulk.

The results presented in this paper underline the power of perturbative metamaterials.²⁸ On one hand, we leveraged this technique to find a first implementation of a quantized quadrupole insulator, a new class of topological materials. On the other hand, the platform of a continuous elastic medium provides a direct route to technological applications for any theoretical idea which can be represented by a tight-binding model.

Acknowledgements We acknowledge financial support from the Swiss National Science Foundation and the NCCR QSIT. TL acknowledges support from a Marie Curie fellowship and ORB the ETH postdoctoral fellowship FEL-26 15-2.

Author contributions SDH conceived the research. MSG, VP and ORB designed the samples. MSG, VP, SDH, and SR conducted the experiments. LGV and TL fabricated the samples.

* These authors contributed equally to this work.

¹ King-Smith, R. D. & Vanderbilt, D. Theory of polarization of crystalline solids. *Phys. Rev. B* **47**, 1651(R) (1993). URL <https://doi.org/10.1103/PhysRevB.47.1651>.

² Taherinejad, M., Garrity, K. F. & Vanderbilt, D. Wannier center sheets in topological insulators. *Phys. Rev. B* **89**, 115102 (2014). URL <https://doi.org/10.1103/PhysRevB.89.115102>.

³ Berry, M. V. Quantal phase factors accompanying adiabatic changes. *Proc. R. Soc. Lond. A* **392**, 45 (1984). URL <http://dx.doi.org/10.1098/rspa.1984.0023>.

⁴ Thouless, D. J., Kohmoto, M., Nightingale, M. & den Nijs, M. Quantized hall conductance in a two-dimensional periodic potential. *Phys. Rev. Lett.* **49**, 405 (1982). URL <http://link.aps.org/doi/10.1103/PhysRevLett.49.405>.

⁵ Kane, C. L. & Mele, E. J. Z_2 topological order and the quantum spin hall effect. *Phys. Rev. Lett.* **95**, 146802 (2005). URL <http://link.aps.org/abstract/PRL/v95/e146802>.

⁶ Chiu, C. K., Teo, J. C. Y., Schnyder, A. P. & Ryu, S.

Classification of topological quantum matter with symmetries. *Rev. Mod. Phys.* **88**, 035005 (2016). URL <https://doi.org/10.1103/RevModPhys.88.035005>.

⁷ v. Klitzing, K., Dorda, G. & Pepper, M. New method for high-accuracy determination of the fine-structure constant based on quantized hall resistance. *Phys. Rev. Lett.* **45**, 494 (1980). URL <http://link.aps.org/doi/10.1103/PhysRevLett.45.494>.

⁸ König, M. *et al.* Quantum spin hall insulator state in hgte quantum wells. *Science* **318**, 766 (2007). URL <http://dx.doi.org/10.1126/science.1148047>.

⁹ Hsieh, D. *et al.* A topological dirac insulator in a quantum spin hall phase. *Nature* **452**, 970 (2008). URL <https://dx.doi.org/10.1038/nature06843>.

¹⁰ Xu, S.-Y. *et al.* Discovery of a weyl fermion semimetal and topological fermi arcs. *Science* **349**, 6248 (2015). URL <https://dx.doi.org/10.1126/science.aaa9297>.

¹¹ Lu, L., Joannopoulos, J. D. & Soljačić, M. Topological states in photonic systems. *Nature Phys.* **12**, 626 (2016).

- ¹² Süssstrunk, R. & Huber, S. D. Observation of phononic helical edge states in a mechanical topological insulator. *Science* **349**, 47 (2015). URL <http://dx.doi.org/10.1126/science.aab0239>.
- ¹³ Süssstrunk, R. & Huber, S. D. Classification of topological phonons in linear mechanical metamaterials. *Proc. Natl. Acad. Sci. USA* **113**, E4767 (2016). URL <https://dx.doi.org/10.1073/pnas.1605462113>.
- ¹⁴ Benalcazar, W. A., Bernevig, B. A. & Hughes, T. L. Quantized electric multipole insulators. *Science* **357**, 61 (2017). URL <https://dx.doi.org/10.1126/science.aah6442>.
- ¹⁵ Nash, L. M. *et al.* Topological mechanics of gyroscopic metamaterials. *Proc. Natl. Acad. Sci. USA* **112**, 14495 (2015). URL <http://dx.doi.org/10.1073/pnas.1507413112>.
- ¹⁶ Liu, Z. *et al.* Locally resonant sonic materials. *Science* **289**, 1734 (2000). URL <http://dx.doi.org/10.1126/science.289.5485.1734>.
- ¹⁷ Huber, S. D. Topological mechanics. *Nature Phys.* **12**, 621 (2016). URL <http://dx.doi.org/10.1038/nphys3801>.
- ¹⁸ Bernevig, B. A., Hughes, T. L. & Zhang, S.-C. Quantum spin hall effect and topological phase transition in hgte quantum wells. *Science* **15**, 1757 (2006). URL <http://dx.doi.org/10.1126/science.1133734>.
- ¹⁹ Fu, L. & Kane, C. L. Time reversal polarization and a z_2 adiabatic spin pump. *Phys. Rev. B* **74**, 195312 (2006). URL <http://link.aps.org/abstract/PRB/v74/e195312>.
- ²⁰ Moore, J. E. & Balents, L. Topological invariants of time-reversal-invariant band structures. *Phys. Rev. B* **75**, 121306(R) (2007). URL <http://link.aps.org/abstract/PRB/v75/e121306>.
- ²¹ Qi, X.-L., Hughes, T. L. & Zhang, S.-C. Topological field theory of time-reversal invariant insulators. *Phys. Rev. B* **78**, 195424 (2008). URL <http://link.aps.org/doi/10.1103/PhysRevB.78.195424>.
- ²² Xiao, M. *et al.* Geometric phase and band inversion in periodic acoustic systems. *Nature Phys.* **11**, 240 (2015). URL <http://dx.doi.org/10.1038/nphys3228>.
- ²³ Rechtsman, M. C. *et al.* Photonic floquet topological insulators. *Nature* **496**, 196 (2013). URL <http://dx.doi.org/10.1038/nature12066>.
- ²⁴ Hafezi, M., Mittal, S., Fan, J., Migdall, A. & Taylor, J. M. Imaging topological edge states in silicon photonics. *Nature Photon.* **7**, 1001 (2013). URL <http://dx.doi.org/10.1038/nphoton.2013.274>.
- ²⁵ Lang, N. & Büchler, H. P. Topological networks for quantum communication between distant qubits. *arXiv:1705.06901* (2017). URL <https://arxiv.org/abs/1705.06901>.
- ²⁶ Benalcazar, W. A., Bernevig, B. A. & Hughes, T. L. Electric multipole moments, topological multipole moment pumping, and chiral hinge states in crystalline insulators. *arXiv:1708.04230* (2017).
- ²⁷ Fidkowski, L., Jackson, T. S. & Klich, I. Model characterization of gapless edge modes of topological insulators using intermediate brillouin-zone functions. *Phys. Rev. Lett.* **107**, 036601 (2011). URL <https://doi.org/10.1103/PhysRevLett.107.036601>.
- ²⁸ Matlack, K. H., Serra-Garcia, M., Palermo, A., Huber, S. D. & Daraio, C. Designing perturbative metamaterials from discrete models: From veselago lenses to topological insulators. *arXiv:1612.02362* (2016). URL <https://arxiv.org/abs/1612.02362>.
- ²⁹ Coulais, C., Teomy, E., de Reus, K., Shokef, Y. & van Hecke, M. Combinatorial design of textured mechanical metamaterials. *Nature* **535**, 529 (2016). URL <http://dx.doi.org/10.1038/nature18960>.
- ³⁰ Su, W. P., Schrieffer, J. R. & Heeger, A. J. Solitons in polyacetylene. *Phys. Rev. Lett.* **42**, 1698 (1979).
- ³¹ Hall, J. J. Electronic effects in the elastic constants of n -type silicon. *Phys. Rev.* **161**, 756 (1967). URL <https://doi.org/10.1103/PhysRev.161.756>.

Methods

Topological quantum number: Nested Wilson loops. Here we use the language of fermions, where bands below a given gap can be “filled”. For the phononic case, one has to replace “filled bands” with “bands below the frequency of interest”. Assuming two bands $n = 1, 2$ are filled, one can use the non-abelian Berry phase $\mathcal{A}_{nm}^x(\mathbf{k}) = i\langle u_m(\mathbf{k}) | \partial_{k_x} | u_n(\mathbf{k}) \rangle$ of the Bloch wave-functions $|u_n(\mathbf{k})\rangle$ to construct the Wilson-loop operators

$$\mathcal{W}_x(k_y) = \text{T exp} \left[i \oint dk_x \mathcal{A}_{nm}^x(\mathbf{k}) \right]. \quad (3)$$

Here, T denotes the path ordering along a closed loop in the Brillouin zone. The eigenvalues $\nu^\pm(k_y)$ of $\mathcal{W}_x(k_y)$ are in one-to-one correspondence to the spectrum of an edge perpendicular to the x -coordinate²⁷ (or perpendicular to y when x and y are interchanged). If the edge modes are gapped, the eigenvectors $v_n^\pm(k_y)$ of $\mathcal{W}_x(k_y)$ can be used to split the filled bands in a well-defined way: $|w_\pm(\mathbf{k})\rangle = \sum_{n=1}^2 v_n^\pm(k_y) |u_n(\mathbf{k})\rangle$. The nested polarization is then defined as

$$p_y^{\nu^\pm} = \frac{1}{(2\pi)^2} \int d\mathbf{k} \mathcal{A}_\pm^y(\mathbf{k}), \quad (4)$$

with $\mathcal{A}_\pm^y(\mathbf{k}) = i\langle w_\pm(\mathbf{k}) | \partial_{k_y} | w_\pm(\mathbf{k}) \rangle$. It can be shown that the presences of two mirror-symmetries M_x and M_y that do not commute are a necessary requirement for the nested polarizations $p_x^{\nu^\pm}$ and $p_y^{\nu^\pm}$ to be quantized to 0 or 1/2.¹⁴

Model. The model shown in Fig. 1c can be expressed with the help of Γ -matrices $\Gamma_k = -\tau_2 \otimes \sigma_k$, $\Gamma_4 = \tau_1 \otimes \sigma_0$, $k = 1, 2, 3$; τ, σ are the standard Pauli-matrices. Using these matrices we can write¹⁴

$$\begin{aligned} \mathcal{D}(k_x, k_y) &= [\gamma_x + \lambda_x \cos(k_x)]\Gamma_4 + \lambda_x \sin(k_x)\Gamma_3 \\ &+ [\gamma_y + \lambda_y \cos(k_y)]\Gamma_2 + \lambda_y \sin(k_y)\Gamma_1 = \sum_{i=1}^4 d_i(\mathbf{k})\Gamma_i. \end{aligned} \quad (5)$$

The C_4 -symmetric version of Fig. 1c is obtained by setting $\lambda_x = \lambda_y$ and $\gamma_x = \gamma_y$. The mirror symmetries are represented by $\mathcal{D}(-k_x, k_y) = m_x \mathcal{D}(k_x, k_y) m_x^\dagger$ and $\mathcal{D}(k_x, -k_y) = m_y \mathcal{D}(k_x, k_y) m_y^\dagger$ with $m_x = \tau_1 \sigma_3$ and $m_y = \tau_1 \sigma_1$, respectively. The eigenvalues of $\mathcal{D}(k_x, k_y)$ are given by $\zeta = \pm|\mathbf{d}(\mathbf{k})|$, leading to two doubly-degenerate bands. Bulk gap-closings occur when $\mathbf{d}(\mathbf{k}) = 0$, which only happens for the C_4 -symmetric case at $\lambda = \pm\gamma$. The spectrum of the mechanical system is given by $\nu = \sqrt{\nu_0^2 + \zeta}$, with a frequency offset ν_0 . Finally, the eigenvectors $|u_n(\mathbf{k})\rangle$ of $\mathcal{D}(k_x, k_y)$ can be used to calculate the Wilson loop operators of Eq. (3). The phase diagram and the evolution of the Wannier bands of model (5) are shown in the Extended Data Fig. 1.

The decay of the edge and corner states into the bulk is simple to derive in analogy to the Su-Schrieffer-Heeger model,³⁰ where the wavefunction has a node on every other site and is exponentially decaying with a decay length of $\xi/a = 2/(\log|\lambda/\gamma|)$ (in units of the site-to-site distance

a). For our ratio of $\lambda/\gamma \approx 0.28$ (see below) this results in $\xi/a \approx 1.6$. In other words, $1 - e^{-4/\xi} \approx 92\%$ of the energy of a edge/corner mode is stored on the outermost row/corner site.

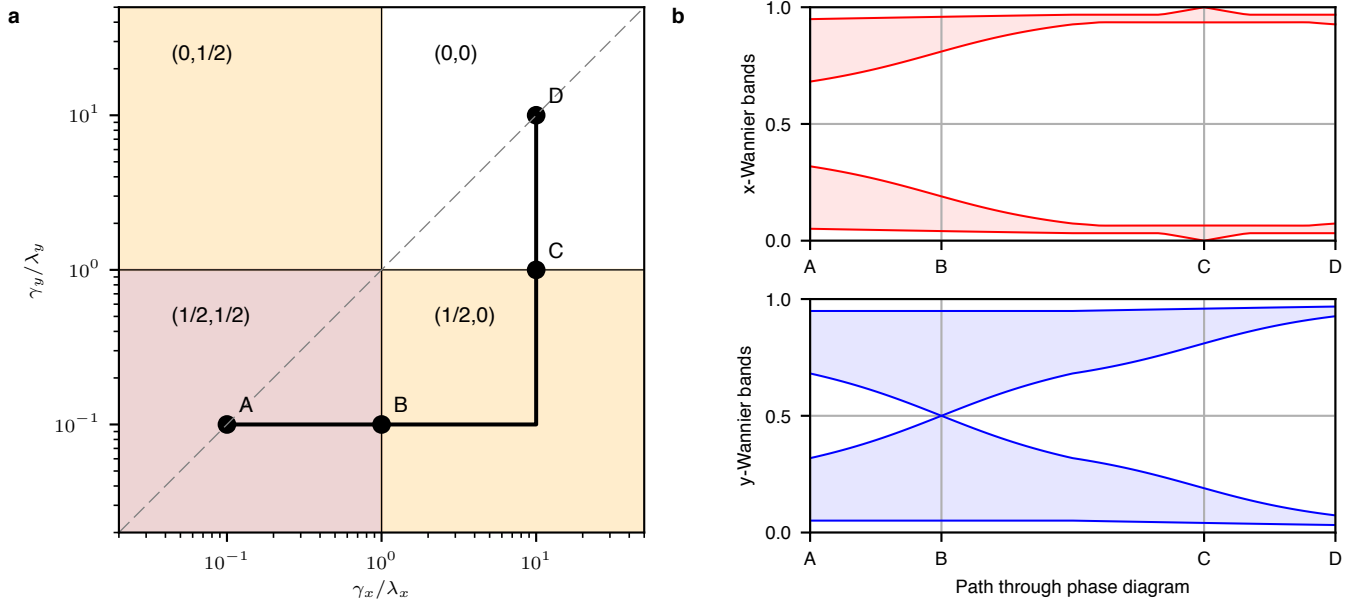
Signal analysis. All measurements are performed with an interferometer (IDS3010 from attocube) after exciting with an ultrasound air-transducer (SMATR300H19XDA from Steiner & Martins Inc). All measurements are subject to a systematic uncertainty of the interferometer of ~ 5 pm, and a statistical error determined by repeated measurements of ~ 10 pm, resulting in an error estimation on the displacements of ~ 11.2 pm. Careful error-propagation analysis results in error bars on all the figures which are smaller than the symbol size. The transducer has an essentially flat frequency response over the frequencies of interest, see Extended Data figure 2 (measured with a second air-transducer). The 0.46 dB variations are negligible with respect to the variations in response of 80 dB.

To remove variations in response due to slight misalignments of the measurement point we normalize the local spectra by $\int d\nu \Delta z_i(\nu) \propto \int d\nu \psi_i^2(\nu)$, as required by the completeness of the eigenmodes. This is only valid under the assumption that all modes suffer from the same loss, or equivalently, have the same quality factor $Q \approx 1000$ (determined from the width of the corner modes). This assumption is justified for the following reason. Dissipation arises from two main sources: the viscoelasticity of the sample and the dissipation into the surrounding air. For both cases all disconnected plates suffer from the same damping. The perturbative nature of our beams (recall the bandwidth of ~ 5 kHz around the center frequency of ~ 74 kHz), restricts also the effects of the couplings on the dissipation. Moreover, our termination is such that all plates see an identical surrounding, independent of their location in bulk, along the edges or on the corners. Moreover, spectra based on data which is not normalized are almost identical to the ones shown in this paper (not shown). Finally, in all figures where arbitrary units are indicated, we normalize to the maximal value shown in the respective figure.

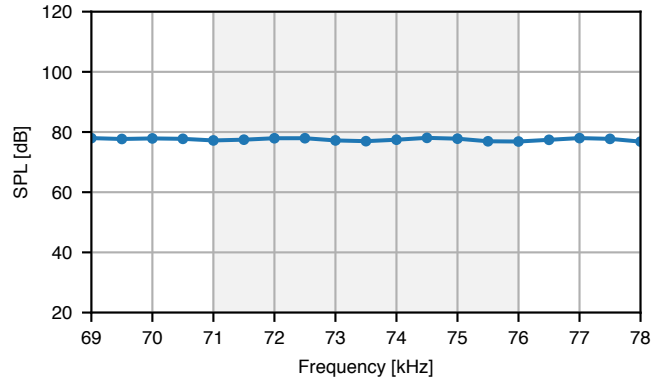
As the bulk, edge, and corner modes spectrally overlap, there is no unique way to separate them in our measurements. However, the fact that the decay length is extremely short ($\xi/a \approx 1.6$, see above), a separation using the filters shown in Fig. 2d, where we simply select sites in the interior, along the edge and the corner sites respectively, is well justified.

Greens functions. In addition to the measurement of $\psi_i^2(\nu)$ by moving the exciter with the measurement point, we can also measure the Greens function $\psi_i(\nu)\psi_j(\nu)$ by fixing the exciter at site j and moving the measurement point i , while exciting at frequency ν .

We first measure the corner Greens function for the four individual corners at their respective frequencies (determined from Fig. 3d). In the Extended Data Fig. 3 we show the results. The density maps show the measured wave function $\psi(x, y)$ (x and y replace the site index i).



Extended data Fig. 1: **Phase diagram.** **a**, Phase diagram of model in Eq. (5). The brown area marks the quantized quadrupole phase, whereas the orange areas are the $(1/2, 0)$ and $(0, 1/2)$ phases with no corner modes but emergent edge physics along two parallel edges. The dashed line indicates the C_4 -symmetric line, where the bulk gap is closing at the phase transition. The transitions away from the C_4 -symmetric line happen through bulk-induced edge-transitions, where no bulk gap is closing. **b**, The evolution of the Wannier bands in x and y direction along the path shown in **a**. The transition from the quadrupole phase to the $(1/2, 0)$ phase is marked by a gap-closing at $1/2$, removing any polarization in the system. The second transition is induced by a gap closing at 0 .



Extended data Fig. 2: **Transducer characterization.** Frequency response of the used ultrasound transducer over the frequency region of interest shaded in gray. The 0.46 dB fluctuations are negligible with respect to the 80 dB variations in the measured response.

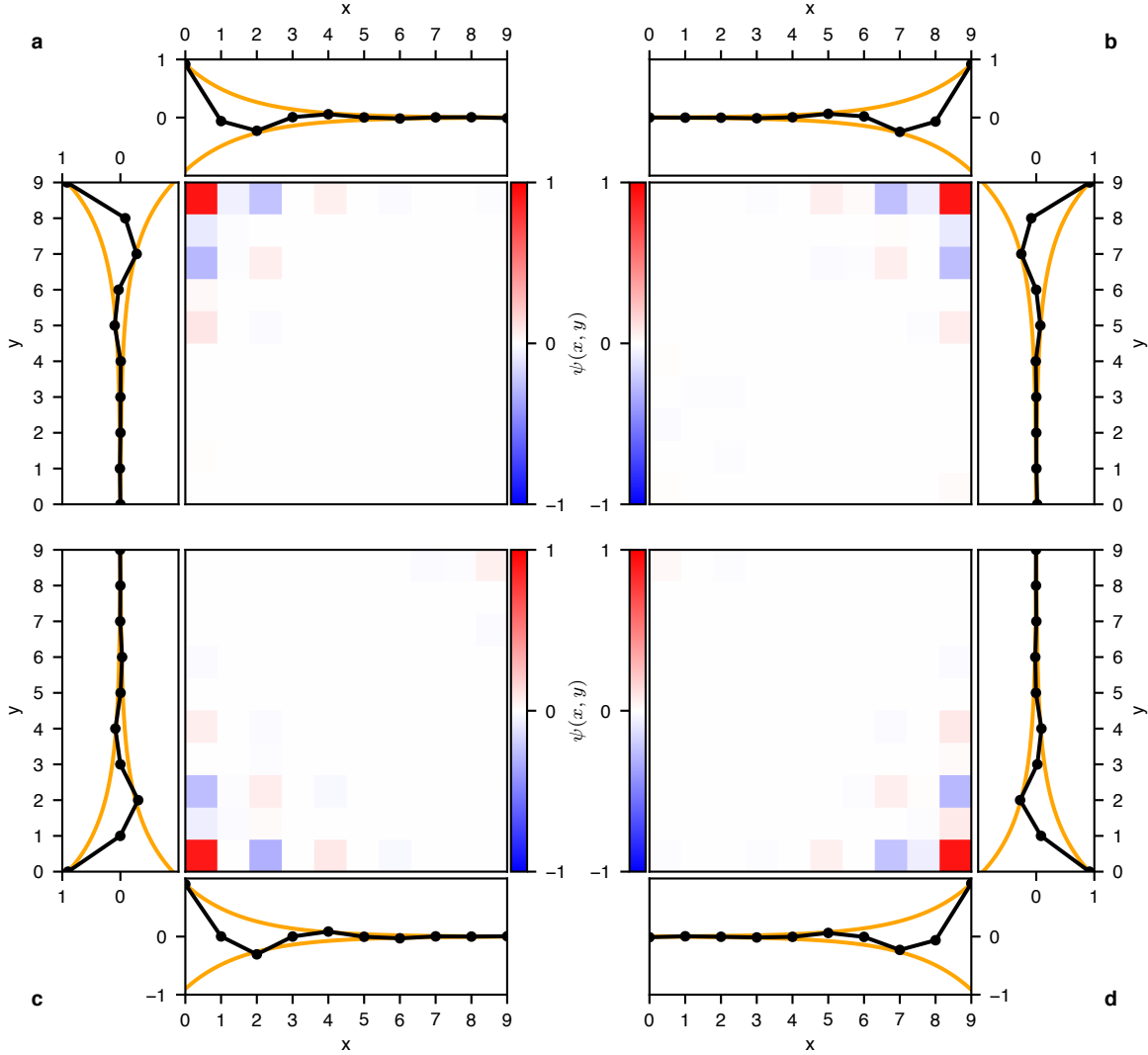
The four panels prove that the four corner modes are independent and the spread in their frequency arises not from their hybridization. Along the edges we show the decay of the wave function and compare their envelope to the theoretical prediction with a decay length $\xi/a \approx 1.6$.

In the Extended Data Fig. 4 we display the analysis of the edge physics by exciting on the bottom left corner and measuring along the lines indicated in the Extended Data Fig. 4a. The goal is to show that we can experimentally determine the sign of the couplings. To this end, we model

our edge states by a simple Su-Schrieffer-Heeger model

$$D(k) = 4\pi^2\nu_0^2 + \sum_{i=1}^2 d_i(k)\sigma_i, \quad (6)$$

where the σ -matrices encode the two sublattices, k is the momentum along the edge; $d_1(k) = \zeta[|\gamma| + |\lambda| \cos(k)]$ and $d_2 = \zeta|\lambda| \sin(k)$. Along the horizontal edge, the couplings are positive $\zeta = 1$, whereas along the vertical edge we have negative matrix elements $\zeta = -1$. The spectrum

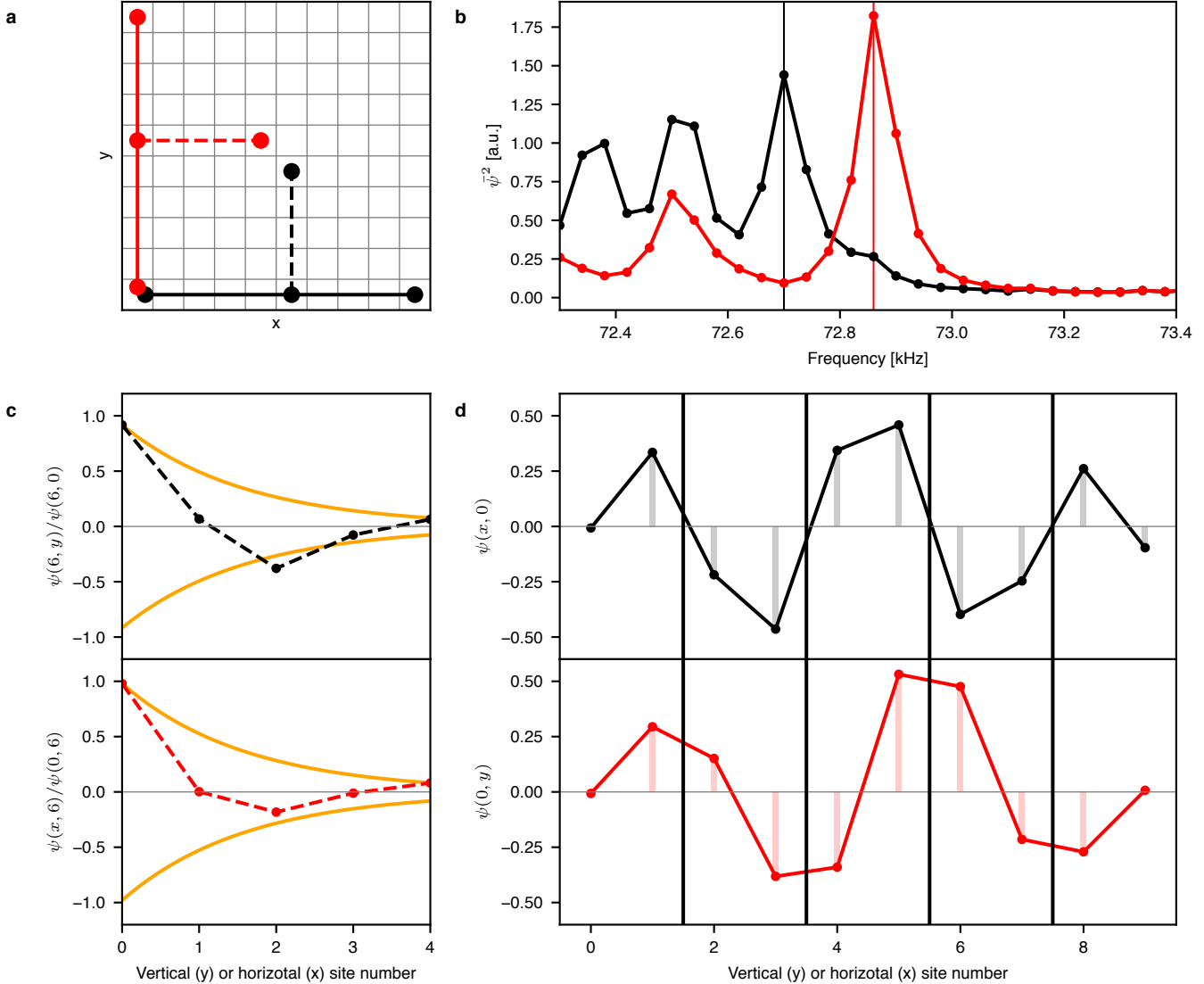


Extended data Fig. 3: **Corner Greens functions.** In the panels **a–d**, the corner plates at $(0,9)$, $(9,9)$, $(0,0)$, $(9,0)$ are excited and the respective edge mode frequency. The recorded response (amplitude and phase) allows to reconstruct the eigenfunctions $\psi(x, y)$ of the individual corner modes. Along each edge, the measured decay of the modes are shown together with the theoretical prediction (orange). Given the decay length $\xi \approx 1.6a$, where a is the lattice constant, the residual weight of maximally 2% on the corners other than the ones excited is stemming from spurious acoustic excitation rather than hybridization.

is given by $\omega_{\pm}(k) = \sqrt{4\pi^2\nu_0^2 \pm \zeta|\mathbf{d}(k)|}$ with associated eigenvectors

$$v_{\pm}(k) = \frac{e^{ikr_i}}{\sqrt{2}} \begin{pmatrix} \pm 1 \\ \frac{d_1(k) + id_2(k)}{|\mathbf{d}(k)|} \end{pmatrix}. \quad (7)$$

Note that the highest frequency modes below the band gap are given by $\omega_-(\pi)$ for $\zeta > 0$ and $\omega_+(\pi)$ for $\zeta < 0$, respectively. For a finite edge, one can build eigenmodes from $v_{\pm}(k)$ that fulfill the desired boundary conditions. Note that the ± 1 in the first component of $v_{\pm}(k)$ deter-



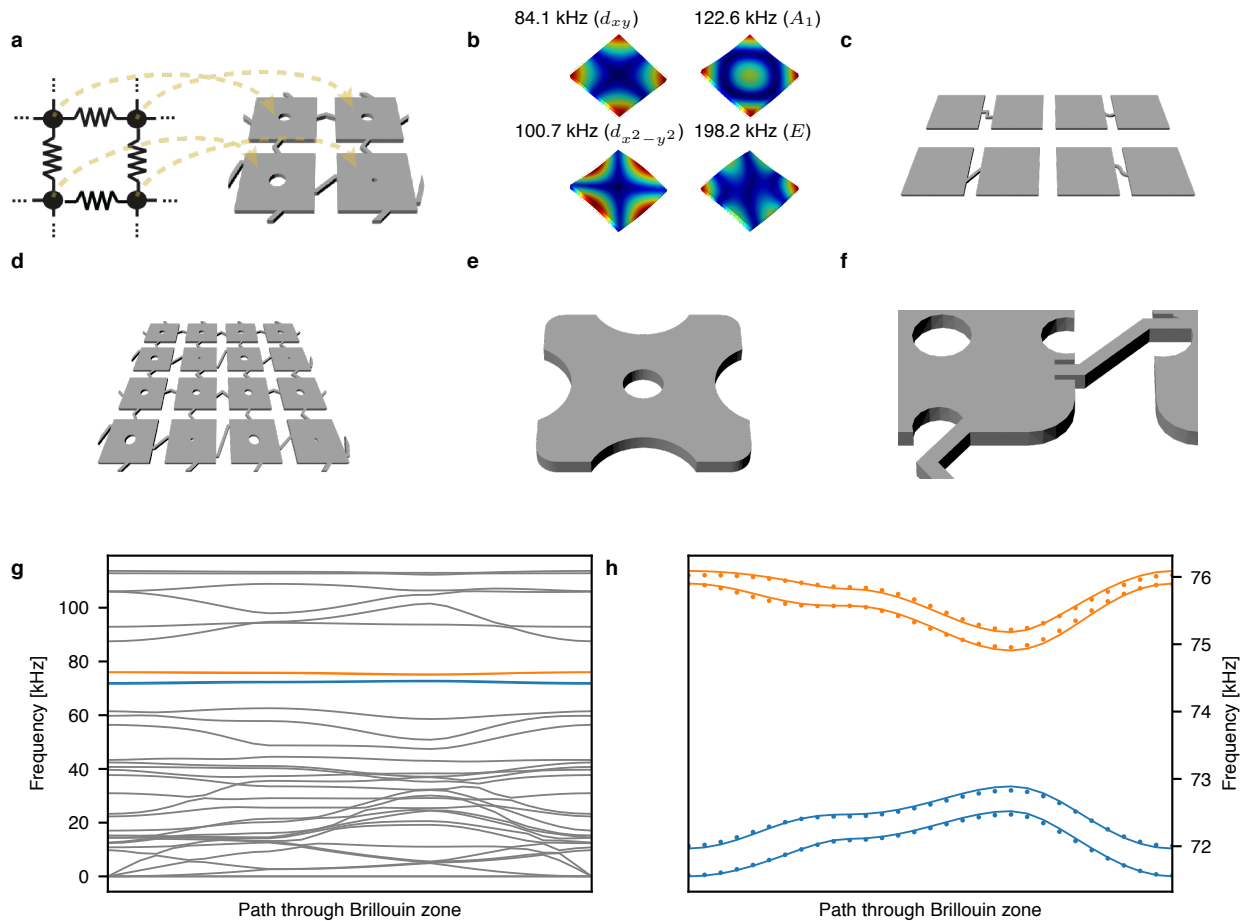
Extended data Fig. 4: **Edge Greens function a**, Sketch of the measured system. The bottom left plate at $(x, y) = (0, 0)$ was excited. **b**, Integrated frequency response $\bar{\psi}^2 = \sum_i \psi^2(\nu)$ where i runs along the red and black edges indicted with a full line in **a**. The two highest frequency peaks below the band-gap shown with vertical lines are analyzed. **c**, The decay of the two edge modes into the bulk along the dashed lines in **a**. The orange lines show the theoretical prediction. **d**, The mode profiles $\psi(x, y)$ along the two edges. The edge with positive couplings has nodes between the unit cells, whereas the edge with negative couplings has nodes inside the unit cell, establishing a direct measurement of the negative couplings giving rise to the π -flux.

mines the relative sign between the mode inside one unit cell. Without specifying the exact boundary conditions, nor using knowledge on the values of γ and λ , we cannot determine this relative sign. However, we can predict that it will be different on edges with $\zeta = \pm 1$.

To find the frequency of the highest mode per edge below the gap we show the integrated weight $\bar{\psi}^2 = \sum_i \psi^2(\nu)$ along the respective edge in the Extended Data Fig. 4b. Fixing the excitation frequencies to the indicated values we measure the edge wave function these modes. The resulting sign change is indeed different (inside vs. between

unit-cells) on the two edges. Finally, to further justify our filtering, we show that also the decay of the edge modes follows the expected decay with $\xi/a \approx 1.6$.

Sample design. The plate geometries investigated in this article have been obtained in the framework of perturbative metamaterials, cf. Extended Data Fig. 5.²⁸ We combine geometric elements (silicon plates, beams and holes) to create a material that reproduces the discrete model of Benalcazar et al. over a range of frequencies. A perturbative metamaterial design consists of repeating basic resonating units (5 mm x 5 mm x 0.364 mm silicon plates)



Extended data Fig. 5: **Perturbative design of a quadrupole topological insulator** **a**, The design approach is based on establishing a correspondence between elements of an objective model and geometric features of the metamaterial. Each degree of freedom of the objective model is mapped into a single plate by expressing the displacement of each plate as a linear combination of free plate modes. **b**, Here, only the first non-rigid body mode with d_{xy} -symmetry is used (top left). **c**, Independent two-plate systems simulated to create an adequate initial guess for the geometry of the system. **d**, Four unit-cell design simulated during the final gradient optimization. **e**, The refined single-plate design removes material at the maximums of nearby higher-order modes. **f**, Small trenches at the junction between beams and plates. These trenches suppress the coupling to higher order modes by avoiding regions where these modes have a large displacement. **g**, Dispersion along high-symmetry lines in the Brillouin zone calculated with the finite-elements method. The bands arising from the d_{xy} mode are highlighted in color. **h**, Detailed view of the spectrum in the frequency range of interest. The dots denote the full finite elements results whereas the lines are calculated from the extracted reduced order model.

that weakly interact with neighbouring resonant units. Here, this weak interaction is implemented using thin silicon beams. The weak interaction has two effects: First, the modes of isolated plates hybridize to Bloch bands of small bandwidth, preventing bands originating from unwanted modes to cross in frequency. Second, the weak interaction allows us to approximate the effect of different geometric elements by adding up individual contributions (See Ref. 28 for details), resulting in a drastic speedup of the calculation times.

The design process starts by establishing a correspondence between the degrees of freedom in the metamaterial and those in the objective discrete model. This is done by expressing the dynamic deformation of the metamate-

rial's basic resonant units (plates) as a linear combination of free plate eigenmodes, see Extended Data Fig. 5b. For sufficiently good spectral separation and sufficiently weak interactions, a single-mode local basis is enough to capture the material response with high precision. Each degree of freedom in the objective model is mapped to a single plate, which is assumed to vibrate in its first non-rigid-body, which for our parameters has d_{xy} symmetry. Then, we evaluate individual coupling beam geometries to identify the most suitable designs and create a database relating beam geometry and coupling strength, obtained by simulating two-beam systems, cf. the Extended Data Fig. 5c. Geometries are evaluated according to three parameters: (i) Ability to attain a broad range of couplings, (ii) low

compressional strength to prevent the in-plane acoustic bands from reaching high frequencies where they could hybridize with the topological band and (iii) absence of beam resonances in the frequency range of interest to exclude retardation effects in the couplings. Once the database has been assembled, we start a design by quickly constructing an approximate material geometry, and then refine it by performing a gradient optimization on a full model, cf. the Extended Data Fig. 5d, that accounts for the interactions between different geometric features.

We extract the effective theory for our design by first calculating the vibrational eigenmodes of a test system (Extended Data Fig. 5c) using the commercial Finite Element Method (FEM) package COMSOL Multiphysics. The eigenmodes' displacements along the three axes u , v and w are then interpolated over a regularly-spaced grid with a pitch of 0.05 mm. This interpolation is done for each mode i and plate j , and denoted by ψ_{ijk} . A similar sampling is also performed for individual free-standing plates and denoted φ_k (here, the index k labels the location and component of the displacement that is being interpolated). Once this information has been extracted from finite element simulations, the displacements of each degree of freedom for each mode are obtained by projecting the test system displacements into single-plate modes, $\alpha_{ij} = (\varphi_l \varphi_l)^{-1} \varphi_k \psi_{ijk}$ (repeated indices denote summation). After this procedure, the components of the matrix α_{ij} contain the displacements of the first non-rigid body mode of the j -th plate for the i -th eigenmode of the test system. The use of an interpolated grid allows us to use an individually optimized mesh for each finite element problem while still being able to express the results of one finite element simulation in terms of another's.

The dynamic matrix K describing the effective theory for the test system is obtained by $K_{lk} = \alpha_{ij} \Omega_{jl}^2 \alpha_{lk}^{-1}$. Here, Ω_{jl}^2 is a diagonal matrix whose elements contain the square angular frequencies of the modes in the frequency range of interest, $\Omega_{ii}^2 = (2\pi f_i)^2$. The resulting matrix K has the same eigenfrequencies and projected eigenmodes as the full system and therefore provides a good description of the system's dynamics. This is highlighted in the Extended Data Fig. 5g/h, which presents a comparison between the dispersion relation obtained from the effective theory and that obtained by solving a full finite-element model under Bloch boundary conditions.

Sample fabrication. The plate and beam geometry of Fig. 1d implements the sought after weak and strong, positive and negative coupling matrix elements. The definition of γ as the hopping strength *inside* a unit cell and λ *between* unit cells renders $\gamma < \lambda$ the non-trivial phase. Connected to this identification is the notion of how we are allowed to terminate the system: Surfaces have to be compatible with the unit-cells, i.e., are not allowed to cut through unit-cells. In turn, this also means we can use the same design of Fig. 1d and realize all phases shown in this paper by starting from a 10×10 sample in the $(1/2, 1/2)$ -phase, then move the cut in y -direction by one row of sites to reach the $(1/2, 0)$ -phase. Finally we move the ter-

mination one column and end up in the $(0, 0)$ -phase. The coupling matrix elements are given by the ratio of the effective mass-density ρ_{eff} of the mode we use and the beam stiffness connecting two plates. We use a $364 \mu\text{m}$ thick Si-wafer in (100) orientation, where we align the x - and y -axis of our model with the in-plane crystalline axes. The mass density of Si is $\rho = 2330 \text{ kg/m}^3$, the Young's moduli $E_x = E_y = E_z = 130 \text{ GPa}$, the Poisson ratios $\nu_{yz} = \nu_{zx} = \nu_{xy} = 0.28$, and the shear moduli $G_{yz} = G_{zx} = G_{xy} = 79.6 \text{ GPa}$.³¹ This results in an offset frequency for our mode of $\nu_0 = 73.895 \pm 0.03 \text{ kHz}$ and the coupling matrix elements are given by $\lambda = 6.69 \pm 0.17 \times 10^9 \text{ (rad/s)}^2$ and $\gamma = 1.89 \pm 0.07 \times 10^9 \text{ (rad/s)}^2$. The error estimation is detailed in the next paragraph.

Our samples are fabricated out of double side polished 100 mm Si-wafers. We measure individually the thickness of each wafer at several spots across the wafer, and we confirm that the overall total thickness variation within each wafer we use is $\leq 1 \mu\text{m}$. We fabricate plate and beam geometries as illustrated in Fig. 1d using standard micro-fabrication techniques. First, $1 \mu\text{m}$ of SiO_2 is grown on the wafers via wet thermal oxidation (to be used as an etch mask), and a $2 \mu\text{m}$ thick layer of Al (that serves to protect the structure once the whole silicon has been removed) is deposited on the backside of the wafers using e-beam evaporation. A patterned $5 \mu\text{m}$ thick photoresist is used as an etch-mask when patterning the front side oxide in a reactive ion etching process. Using the remaining photoresist and the underlying oxide as etch masks, we etch through the wafer with a deep reactive ion etching following a Bosch[®] process alternating etching and passivation cycles. The ratio between both cycles is chosen to yield vertical side walls. This angle is characterized in several points of each wafer, confirming a variation of the angle of $\leq 2.5^\circ$. The Si etching terminates when reaching the backside oxide. The resulting oxide/aluminum membranes suspended between the beams and plates are removed by wet etching first the aluminum and then the oxide. This latter step also removes any oxide leftovers present on the front side. The main sources of errors in the targeted model arising from the sample fabrication are: (i) Total thickness variation – which we characterize being smaller than $1 \mu\text{m}$, and therefore stands for less than a 0.3% variation across the wafer. (ii) Different sidewall angles between different parts of the wafer – we measure it to be smaller than 2.5° . Hence, variation in feature sizes, when comparing front side to backside, may be up to $32 \mu\text{m}$. For the width of the plates this corresponds to an error of 0.3%. Finally, (iii) the misalignment of the array with the material crystalline axis (100) . This error has two sources, (a) wafer specifications indicate that the flap is located within $\pm 0.5^\circ$, and (ii) alignment during lithography, which the specifications of our machine states around $\pm 1^\circ$. In either case, this results in an overall error of less than 0.1% in the Youngs modulus. This error leads to the stated uncertainties in the local plate frequencies and couplings using standard elasticity theory. Finally, the wafers are clamped between two steel plates (each of

3 mm thickness), cf. Fig. 2c. The impedance miss-match between the steel plates and the wafer leads essentially to

fixed boundary conditions $\Delta z = 0$.